ACS APPLIED MATERIALS & INTERFACES

Research Article

www.acsami.org

Ni Layer Thickness Dependence of the Interface Structures for Ti/Ni/Ti Trilayer Studied by X-ray Standing Waves

Wenbin Li,[†] Jingtao Zhu,[†] Haochuan Li,[†] Zhong Zhang,[†] Xiaoying Ma,[†] Xiaoyue Yang,[†] Hongchang Wang,[‡] and Zhanshan Wang*,[†]

[†]Key Laboratory of Advanced Micro-structure Materials, MOE, Institute of Precision Optical Engineering, Department of Physics, Tongji University, Shanghai 200092, China

[‡]Diamond Light Source Ltd., Harwell Science and Innovation Campus, Didcot, Oxfordshire OX11 0DE, United Kingdom England

ABSTRACT: X-ray standing waves generated by periodic multilayers have been used to characterize the interface microstructures of Ti/Ni/Ti trilayers based on the X-ray reflectivity (XRR) and grazing incidence X-ray fluorescence (GIXRF) methods. For the Ni layer having thickness of 1.7 nm, it is observed that the roughness of Ti-on-Ni interface is 0.64 nm and that of Ni-on-Ti interface is 0.40 nm, which can be explained by an additional roughness on the Ti-on-Ni interface induced by the nucleation of Ni crystallites when the Ni layer thickness is at the amorphous-to-crystalline transition region. For the Ni layer thickness of 3.3 nm beyond this transition region, the roughness of Ti-on-Ni interface is 0.42 nm and Ni-on-Ti interface is 0.46 nm, which is consistent with the expectation on wetting and dewetting conditions.

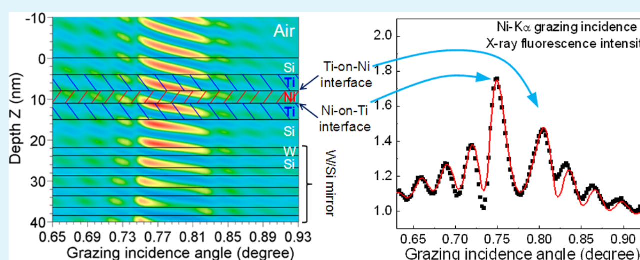

KEYWORDS: *Ni/Ti multilayer, X-ray standing waves, interface structure, X-ray diffraction, GIXRF, XRR*

■ INTRODUCTION

As an important optical element, artificial multilayer of Ni/Ti has been widely applied in the research fields of neutron optics[1,2] and soft X-ray optics.[3,4] For these applications, the reflectivity is one of the most important properties, which is strongly affected by the interface structures. The interface structures for a multilayer depend on the types of alternative deposited materials, the diffusive and reactive properties of these materials and the deposition condition.[5] Concerning Ni/Ti multilayer, the Ti-on-Ni interface is generally smoother than the Ni-on-Ti interface because of smaller surface free energy of Ti than that of Ni.[6] Besides the surface free energy, it was demonstrated that the interface roughness also depends on the thickness of the deposited material.[7,8] For the application of Ni/Ti supermirrors, hundreds of different periodic thicknesses are needed to be deposited for optimum performance. Thus, it is significant to understand how the interface structure is modified with respect to the changes of the Ni layer thickness. Many researchers are interested in making the interface smoother by adding surfactants or barrier layers, such as Ag, Cr, and C.[6,9−11] More attention has also been paid to the study of solid state reaction, the changes of the interface structures and magnetic properties on the annealed Ni/Ti multilayer systems.[12−18] However, the changes of interface roughness with the variation of the Ni layer thickness have not been reported.

For investigating the interface properties, various techniques can be used, such as grazing incidence X-ray reflectivity, transmission electron microscopy (TEM), conversion electron Mössbauer spectroscopy, and so on.[18−20] Due to the limited sensitivity or depth resolution, these traditional approaches may not be able to resolve the true interface. X-ray standing wave has widely been used as a nondestructive probe for characterizing multilayer thin films and elements depth distributions.[21−26] It was demonstrated that X-ray standing wave is capable of investigating the interface structures of thin films with a depth resolution of a fraction of a nanometer.[27] In this study, we investigate the variation of interface structures of Ti/Ni/Ti trilayers with respect to different thickness of Ni layer by using X-ray standing waves. It is found that the roughness of Ni-on-Ti was kept almost the same when the Ni layer thickness changed from 1.7 to 3.3 nm, but the interface of Ti-on-Ni became less rough, which are explained to be related with the amorphous-to-crystalline transition in the Ti/Ni/Ti trilayer.

■ EXPERIMENTAL DETAILS

For characterizing the interface structures of Ti/Ni/Ti trilayer, the multilayer structure is designed as Si(Sub)/[W(2.0 nm)/Si(2.9 nm)] × 20/Si(3.9 nm)/Ti(4.0 nm)/Ni(3.0 nm)/Ti(4.0 nm)/Si(4.0 nm) (designated as ML1), which is shown in Figure 1. In this multilayer, 20 periods of bilayers of W(2.0 nm)/Si(2.9 nm) were used as a substrate to generate the X-ray standing waves by varying the grazing incidence angle across the first Bragg peak region. On top of the W/Si periodic multilayer, a Ti/Ni/Ti sandwich structure was deposited with a covering layer Si(4.0 nm) for protecting the underlying layers. Between the W/Si multilayer and the Ti/Ni/Ti trilayer, a spacer layer of Si(3.9 nm) was inserted, whose thickness was optimized so that two interfaces of Ni layer can interact individually with the X-ray standing

Received: October 26, 2012
Accepted: December 17, 2012
Published: December 17, 2012

 © 2012 American Chemical Society

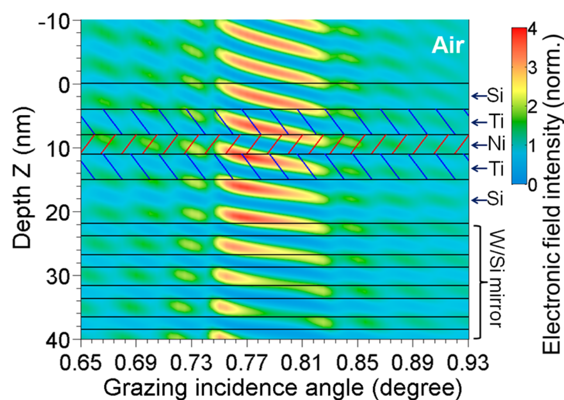

Figure 1. Contour plot of X-ray intensity distributions as a function of grazing incidence angle and depth for ML1 multilayer at X-ray photon energy of 10 keV.

wave antinodes at different incident angles as shown in Figure 1. For characterizing the changes of the interface structure with respect to the thickness variation, another multilayer system designated as ML2 was also fabricated with the structure of Si (Sub)/[W (1.2 nm)/Si (1.2 nm)] × 20/Ti (4.2 nm)/Ni (1.5 nm)/Ti (4.0 nm)/Si (4.0 nm). Since this Ni layer is thinner than that of ML1 specimen, so the underlying W/Si periodic multilayer has a short modulation period length.

With the fabrication of ML1 and ML2 specimens, two other W/Si periodic multilayers (designated as PML1 and PML2) were also fabricated without covering the trilayer. The specimen PML1 (PML2) has the same designed periodic structures as the substrate of ML1 (ML2) for deposing Ti/Ni/Ti trilayers. It was aimed to use the structural parameters of PML1 and PML2 to determine that of the underlying [W/Si] × 20 substrates of ML1 and ML2 specimens, respectively. All multilayer samples were deposited onto polished silicon wafers (100) using DC magnetron sputtering method. The base pressure inside the chamber is better than 2.0×10^{-4} Pa before deposition. Argon with purity of 99.99% was used as the sputtering gas and the working pressure were kept at about 0.13 Pa during deposition.

Grazing incidence X-ray reflectivity and angle-dependent grazing incidence X-ray fluorescence (GIXRF) were simultaneously carried out by using unfocused X-ray beam on B16 beamline at Diamond Light Source, which has been described in detail in our previous work.[28] Briefly, monochromatic X-rays of energy 10 keV from a Si(111) double-crystal monochromator were used in this experiment, which is beyond the *K* absorption edges of Ti and Ni elements. Grazing incident X-ray reflectivity measurements were performed in the θ–2θ geometry by using an avalanche photodiode detector (APD), which has very high count rate and large dynamic range. The characteristic fluorescence radiations from Ti and Ni were collected simultaneously by a Vortex spectroscopy detector placed normal to the sample surface. Before the entrance of the fluorescence detector, an Al pinhole collimator was used to maintain a constant solid angle of detection at various incident angles. The crystalline phases of Ni and Ti layers in ML1 and ML2 were also investigated using large-angle X-ray diffraction (XRD), from which the size of crystallites in Ni layer were determined. This information was combined with the results from XRR and GIXRF methods to analyze the changes of the interfacial structures with respect to the Ni layer thickness variation.

RESULTS AND DISCUSSION

The reflectivity data of ML1 measured at 10 keV photon energy is shown in Figure 2a, where Bragg peaks up to four orders are clearly seen in the experimental curve. The reflectivity profile of ML1 is dominated by the underlying W/Si multilayer and the top layers of Ti/Ni/Ti/Si produce only small modulations on the profiles below the first Bragg peak. So, it is difficult to get the reliable layer thickness and interface roughness of Ti, Ni, and Si layers by just fitting this reflectivity curve with many fitting parameters needed to be optimized. Thus, X-ray reflectivity measurement was first carried out on the periodic multilayer PML1, which has the same structure as the underlying W/Si substrate of ML1 for generating X-ray standing waves. The measured reflectivity data and the fitting curve for PML1 are given in Figure 2b. The fitting reflectivity data were calculated based on Parratt's formalism.[29] The average thickness, the density, and the average interface roughness of W and Si layers were used as the fitting parameters. The fitting results provide the thickness of W layer of 1.89 ± 0.05 nm, Si layer of 3.02 ± 0.05 nm, and the average interface roughness of 0.38 ± 0.05 nm. These parameters obtained were then chosen as initial values for fitting the reflectivity curve of ML1. It was found that these values fitted quite well with the ML1 reflectivity and fluorescence data with changes less than ±0.05 nm, which is similar to the fitting error. As mentioned above, the XRR data cannot provide the reliable parameters of Ti/Ni/Ti sandwich structure alone. However, the angle-dependent fluorescence intensities of Ti and Ni are more sensitive on the depth profiles of elements, which are related with the corresponding layer thickness and the interface roughness. Therefore, the simultaneous fitting on the reflectivity and fluorescence data should be able to provide more reliable structural information than that from XRR fitting only.

Figure 3 gives the measured Ni–Kα and Ti–Kα fluorescence intensities for ML1 specimen over the angle region covering the first-order Bragg peak. The raw fluorescence data have been

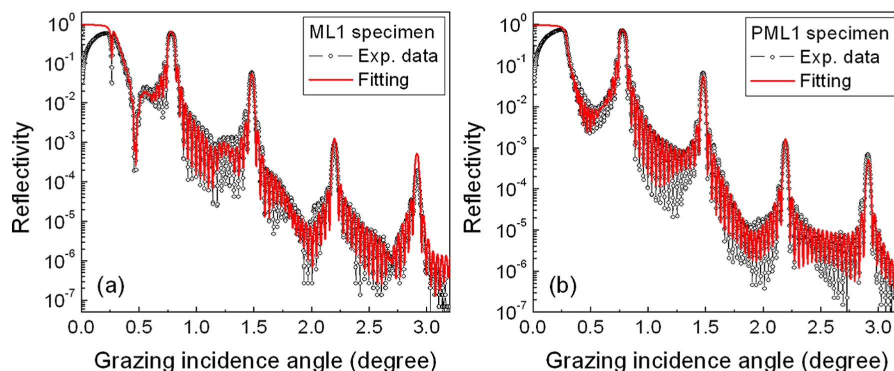

Figure 2. Grazing incidence X-ray reflectivity profiles of (a) ML1 and (b) PML1 multilayers at X-ray photon energy of 10 keV. The open circles represent the measured data, and the solid curves represent the best fitting results.

dx.doi.org/10.1021/am3024614 | ACS Appl. Mater. Interfaces 2013, 5, 404–409

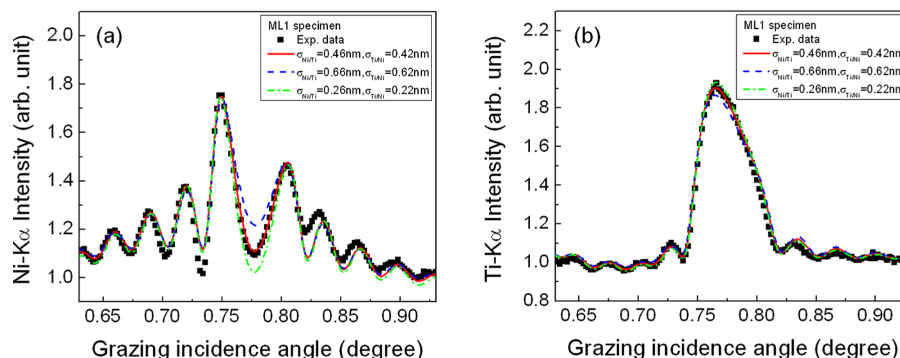

Figure 3. (a) Ni−Kα fluorescence intensity and (b) Ti−Kα fluorescence intensity in the vicinity of first-order Bragg peak for ML1 specimen. The solid squares represent the experimental data for Ni−Kα and Ti−Kα, respectively. The continuous curves represent the best fits to the experimental data with the roughness of Ni-on-Ti interface $\sigma_{Ni/Ti}$ = 0.46 ± 0.10 nm and that of Ti-on-Ni interface $\sigma_{Ti/Ni}$ = 0.42 ± 0.10 nm. For comparison, the dotted lines represent the simulated fluorescence intensities with the roughness of $\sigma_{Ni/Ti}$ = 0.66 nm and $\sigma_{Ti/Ni}$ = 0.62 nm. The dashed lines represent the simulated fluorescence intensities with the roughness of $\sigma_{Ni/Ti}$ = 0.26 nm and $\sigma_{Ti/Ni}$ = 0.22 nm.

corrected for the footprints and the instrumental geometry.[28] For the Ni−Kα fluorescence intensity, small troughs and peaks are presented below and above the first-order Bragg peak due to the small Kiessig oscillations, which is closely correlated with the reflectivity profiles at the same angle region. Besides these small oscillations, two noticeable enhancements on Ni−Kα fluorescence intensity profile can be observed in the Bragg region from 0.73° to 0.83° in Figure 3a. On the contrary, there is only one broad peak for the profile of Ti fluorescence intensity in the same angular region as shown in Figure 3b. These fluorescence intensity profiles can be illustrated by the formation of X-ray standing waves in the first-order Bragg peak region. When considering a plane electromagnetic wave with *s* polarization incident on a multilayer structure, the X-ray field intensity $I_j(\theta,z)$ at the depth z for the grazing incidence angle of θ is given by[26]

$$I_j(\theta, z) = |E_j^t(0)|^2\left[\exp\{-2k''_{j,z}z\} + \left|\frac{E_j^r(0)}{E_j^t(0)}\right|^2 \exp\{2k''_{j,z}z\} + 2\left|\frac{E_j^r(0)}{E_j^t(0)}\right| \cos\{\nu(\theta) + 2k'_{j,z}z\}\right] \quad (1)$$

where $E_j^t(0)$ and $E_j^r(0)$ are the transmitted and reflected electric field at the top of the jth layer, and $\nu(\theta)$ is the phase of the E field ratio $E_j^r(0)/E_j^t(0) = |E_j^r(0)/E_j^t(0)| \exp(i\nu(\theta))$. The parameters of $k'_{j,z}$ and $k''_{j,z}$ represent the real and imaginary parts of the z-component of the wave vector $k_{j,z} = 2\pi/\lambda(\varepsilon_j - \cos^2\theta)^{1/2}$, where ε_j is the complex dielectric constant of the jth layer medium. By using this formula, the X-ray field intensity distributions were calculated and presented as a contour plot in Figure 1 for ML1 structure in the grazing incidence angle region from 0.66° to 0.93°. As seen from the contour plot, one antinode of the X-ray standing wave partially overlaps with the Ni-on-Ti interface at the angle of 0.76°, which enhances the Ni fluorescence intensity and results in the strongly enhanced peak at the same angle as shown in Figure 3a. When increasing the grazing incidence angle further, this antinode moves out of the Ni layer region toward to the substrate, while the next antinode has not reached the Ti-on-Ni interface. So, Ni−Kα fluorescence intensity decreases and one dip appears in the profile. As the angle is increased further to 0.81°, the X-ray standing wave moves inside the multilayer and the next antinode partially overlaps with the Ti-on-Ni interface, which results in another peak in Ni−Kα fluorescence intensity profile at 0.81°. For the Ti−Kα fluorescence intensity, there is always one antinode existing in the upper or the lower Ti layer as observed in Figure 1. Therefore, it gives rise to a broad peak in the profile of Ti−Kα fluorescence intensity in the vicinity of the first Bragg peak. By simulation, it is found that the shapes of these two Ni−Kα fluorescence peaks are sensitive to the interface roughness of Ni-on-Ti and Ti-on-Ni interfaces. Gupta et al. have used this X-ray standing waves technique to identify the Tb/Fe and Cr/Fe interface structures and demonstrated the two interface roughnesses can be unambiguously indentified.[27]

In order to fit the experimental data, the angle-dependent fluorescence intensity is calculated by using fundamental parameter approach.[26,30] According to this approach, the intensity of the primary fluorescence emitted by atom of element x from the sample can be written as

$$F_x(\theta) = \sum_{j=1}^{n} S_{x,E_0} \exp\left[-\sum_{n=1}^{j-1}\frac{(\mu/\rho)_{n,E}\rho_n d_n}{\sin\varphi}\right] \times \int_0^{d_j} C_{j,x}(z) I_j(\theta, z) \exp\left(-\left[\frac{(\mu/\rho)_{j,E}}{\sin\varphi}\right]\rho_j z\right) dz \quad (2)$$

where $F_x(\theta)$ represents the total fluorescence intensity, which is the sum of contributions from individual layers corrected by the absorption from the upper layers. S_{x,E_0} is the X-ray fluorescence production cross-section for element x at photon energy of E_0.[30] ρ_j is the density of layer j and $(\mu/\rho)_{j,E}$ represents the mass attenuation coefficient for the considered fluorescence line with characteristic energy of E. φ is the emission angle of the detected fluorescence X-rays from the specimen surface, which in our case is 90°. $I_j(\theta,z)$ is the field intensity at the depth z. $C_{j,x}(z)$ is the concentration distribution of element x as a function of depth z. Across the interface, the concentration distribution is given by

$$C_{j,x}(z) = \frac{1}{2}\left[1 + \mathrm{erf}\left(\frac{z}{\sqrt{2}\sigma}\right)\right] \quad (3)$$

where σ is the interfacial roughness.[26] It can be seen from eq 2 that, if the field intensity $I_j(\theta,z)$ is mainly determined by the underlying periodic multilayer, the fluorescence intensity will be

more sensitive to the concentration profile of $C_{j,x}(z)$, which is correlated with the interface roughness.

In this study, the reflectivity profile and the fluorescence intensities of Ni−Kα and Ti−Kα have been measured simultaneously, which are then fitted concurrently to get the reliable layer thickness and interface roughness. For the fitting process, the initial structural parameters of W/Si periodic mirror substrate in ML1 have been determined based on the fitting results from PML1 as shown in Figure 2b. This fitting approach is very helpful for searching the best optimized parameters since the initial parameters are in good agreement with the best optimized values within the fitting errors. So, the main variable parameters are the individual layer thickness, surface/interface roughness of Ti/Ni/Ti/Si structure. As shown in Figures 2 and 3, the best fitting gives the layers thickness of Ti (3.9 ± 0.1 nm)/Ni (3.3 ± 0.1 nm)/Ti (3.8 ± 0.1 nm), the roughness of Ti-on-Ni interface equal to 0.42 ± 0.10 nm and that of Ni-on-Ti interface equal to 0.46 ± 0.10 nm, which are listed in Table 1. For comparison, the simulated fluorescence intensity with roughness $\sigma_{Ni/Ti}$ = 0.66 nm, $\sigma_{Ti/Ni}$ = 0.62 nm, and $\sigma_{Ni/Ti}$ = 0.26 nm, $\sigma_{Ti/Ni}$ = 0.22 nm are also shown as the dashed and dashed−dotted curves in Figure 3. The sensitivity of this method is demonstrated by the differences for these Ni−Kα fluorescence profiles, especially at the first-order Bragg peak region. Though the Ti−Kα fluorescence profile are not sensitive on the roughness of Ni/Ti interfaces, it is strongly affected by the individual layer thickness of Ti/Ni/Ti structure and the height of Ti/Ni/Ti relative to the top of W/Si multilayer. So, the simultaneous fitting on three different angle-dependent experimental data, viz., XRR, Ni−Kα, and Ti−Kα fluorescence profiles, should provide more reliable structural parameters than that from XRR only.

Table 1. Roughnesses of Ti-on-Ni and Ni-on-Ti Interfaces and Thicknesses and the Crystallite Size of the Ni Layer for ML1 and ML2 Samples

sample	thickness of Ni layer (nm)	crystallite size of Ni (nm)	$\sigma_{Ti/Ni}$ (nm)	$\sigma_{Ni/Ti}$ (nm)
ML1	3.3 ± 0.1	2.5 ± 0.1	0.42 ± 0.10	0.46 ± 0.10
ML2	1.7 ± 0.1	1.9 ± 0.1	0.64 ± 0.10	0.40 ± 0.10

For characterizing the interface structures of thinner Ni layer, the X-ray reflectivity and fluorescence intensities measurements were carried out on ML2 specimen. Figure 4a, c, and d gives the X-ray reflectivity, Ni−Kα, and Ti−Kα fluorescence intensities for ML2 as a function of grazing incidence angles, respectively. By using the same data processing procedure as done on ML1, the reflectivity curve and the Ni−Kα and Ti−Kα fluorescence intensity profiles of ML2 are simultaneously fitted, while the fitting parameters of the underlying W/Si substrate in ML1 were first determined from PML2 as shown in Figure 4b. The best fitting gives the structural parameters for the multilayer ML2 as [W (1.28 ± 0.05 nm)/Si (1.20 ± 0.05 nm)] × 20/Si (1.4 ± 0.1 nm)/Ti (4.2 ± 0.1 nm) /Ni (1.7 ± 0.1 nm) /Ti (4.4 ± 0.1 nm) /Si (4.8 ± 0.1 nm). The interface roughness of Ti-on-Ni equals 0.64 ± 0.10 nm, and that of Ni-on-Ti equals 0.40 ± 0.10 nm. For demonstrating the sensitivity of this fitting, the dashed curve gives the simulated fluorescence pattern with roughness of $\sigma_{Ni/Ti}$ = 0.64 nm and $\sigma_{Ti/Ni}$ = 0.40 nm compared with the experimental data as shown in Figure 4c and d. One

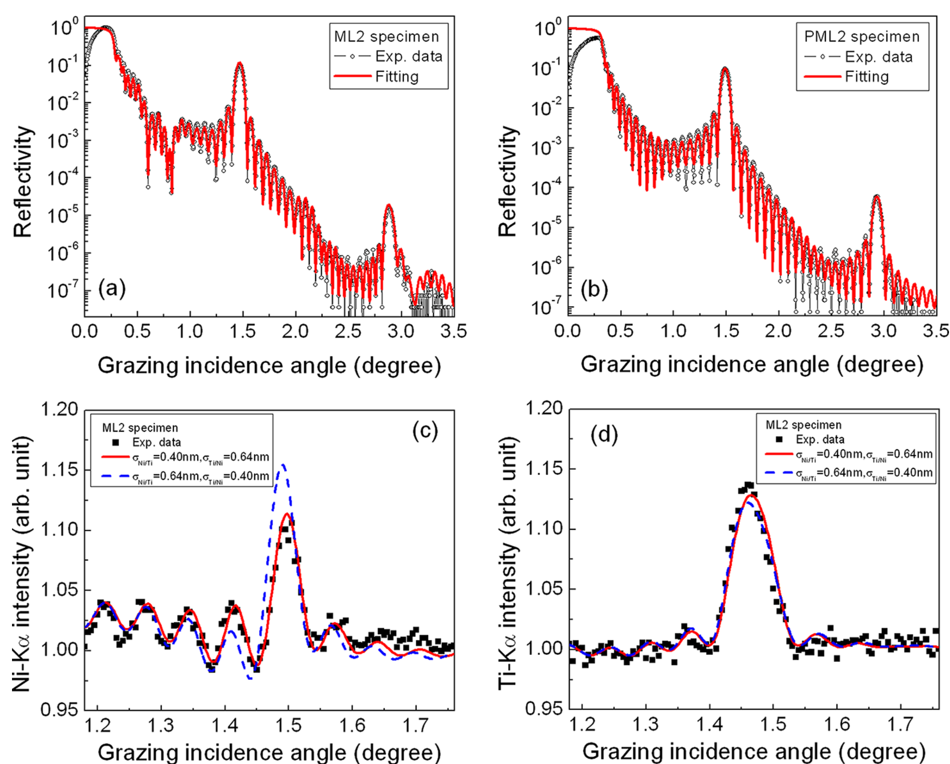

Figure 4. Grazing incidence X-ray reflectivity profiles of (a) ML2 and (b) PML2 multilayers at X-ray photon energy of 10 keV, where the open circles represent the measured data and the solid curves represent the best fitting results. The fluorescence intensities of (c) Ni−Kα and (d) Ti−Kα for ML2, where the solid curves represent the best fits to the experimental data with the roughness of $\sigma_{Ni/Ti}$ = 0.40 ± 0.10 nm and $\sigma_{Ti/Ni}$ = 0.64 ± 0.10 nm. For comparison, the dashed curves represent the simulated fluorescence patterns with the roughness of $\sigma_{Ni/Ti}$ = 0.64 nm and $\sigma_{Ti/Ni}$ = 0.40 nm.

can note that Ti-on-Ni interface is rougher than that of Ni-on-Ti interface when the thickness of Ni layer changes from 1.7 to 3.3 nm. The difference on the roughness of Ti-on-Ni interface cannot be explained by the wetting condition for the growth of Ti on Ni because of the different surface free energy ($\gamma_{Ni} > \gamma_{Ti}$). Thus, it is needed to investigate the changes of the microstructures of Ni layer when Ni layer thickness is changed from 1.7–3.3 nm.

For identifying the crystalline structures, the X-ray diffraction measurements were carried out on the multilayer samples of ML1 and ML2 in the symmetric Bragg–Brentano geometry at photon energy of 10 keV. As shown in Figure 5, two diffraction

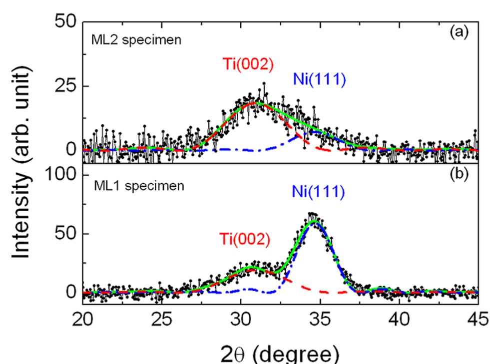

Figure 5. X-ray diffraction patterns measured at X-ray photon energy of 10 keV for specimens of (a) ML2 and (b) ML1.

peaks are presented in the angle region from 26° to 38°, which correspond to the phases of Ti(002) and Ni(111), respectively. These diffraction peaks suggest a crystalline nature of the deposited Ni and Ti layer for ML1 and ML2 specimens. In Figure 5, one may note that the peak position of Ni(111) is shifted toward lower angle compared to that of bulk materials, which was also observed by Clemens.[12] Since there is little chance that Ni_3Ti is formed in the present case, it is possibly caused by the increase of Ni lattice spacing upon the dissolution of Ti into Ni layer as proposed by Hollanders et al.[13] For estimating the crystallite dimensions along the growth direction of multilayer, the following formula[8] was used

$$I(2\theta) = A\frac{\sin^2[\pi/\lambda L(2\theta - 2\theta_B)\cos\theta_B]}{\sin^2[\pi/\lambda d(2\theta - 2\theta_B)\cos\theta_B]} \quad (4)$$

where d is the interplanar distance, L represents the crystallite size, λ is the wavelength (0.124 nm) of the X-ray beam, and $2\theta_B$ is the position of the diffraction peak. By using formula 4, the XRD pattern for ML1 specimen was first deconvolved into two peaks, which represents the Ti(002) and Ni(111) diffraction peaks as shown in Figure 5b. From the fitting results on ML1 specimen, the positions of Ti(002) and Ni(111) diffraction peaks were determined to be at 30.92° and 34.67° with the crystallite sizes L in the growth direction of 1.5 and 2.5 nm, respectively. When fitting the XRD pattern of ML2 specimen, the positions of the Ti(002) and Ni(111) diffraction peaks were fixed to the ones determined from ML1 specimen. From the best fitting results, the average thicknesses of the Ti and Ni crystallites in the growth direction were determined to be 1.5 and 1.9 nm, respectively. As shown in Figure 5a, the fitting curve is in good agreement with the experimental results. It can be seen that the ML1 (T_{Ni} = 3.3 nm) has a smaller crystallite size in the growth direction than the layer thickness, while the ML2 (T_{Ni} = 1.7 nm) may have the average crystallite size a little bit larger than the layer thickness.

It is well-known that above a certain critical thickness the crystallites may nucleate in the magnetron sputter or electron-beam deposited films.[8,16] For this study, we can infer that the critical thickness for the nucleation of Ni crystallites is at about 1.9 nm, which is based on the fact that the Ni(111) diffraction peak existed in the XRD pattern of ML2 with much low intensity. When depositing ML2, though the Ni layer has the average layer thickness less than the critical thickness, the Ni crystallites can nucleate at some positions where the critical thickness is reached due to the statistically random roughness of the Ni layer. Therefore, the crystallites of Ni layer at some isolated positions will introduce additional roughness at the Ti-on-Ni interface. While the Ti-on-Ni interface is expected to be smoother than the Ni-on-Ti interface due to different surface free energy of Ti and Ni, it is found that, when the thickness of Ni layer is close to the critical thickness, the Ti-on-Ni interface is rougher than the Ni-on-Ti interface due to the crystallization of Ni layer. Bajt et al. have also observed the same microstructure changes at the interfaces of Mo/Si multilayers and proposed a model of amorphous-to-crystalline transition to explain it.[8] For ML1 specimen, the thickness of the Ni layer is well above the amorphous-to-crystalline transition region and exceeds the critical thickness everywhere in the layer. Therefore, the Ni layer is mostly polycrystalline for ML1, which is also justified by the stronger Ni(111) diffraction intensity than that of ML2. Then, there is less roughness associated with the Ti-on-Ni interface. When the Ni layer thickness is well beyond the amorphous-to-crystalline transition region, the interface roughness should be dominated by the surface free energy of the deposited materials.

CONCLUSIONS

In this study, the X-ray standing waves method was used to investigate the two interface structures of Ti/Ni/Ti trilayers with different Ni layer thicknesses. When the thickness was at 1.7 nm, which is close to the critical thickness for crystallite formation, the Ti-on-Ni interface was found to be rougher than that of the Ni-on-Ti interface. This is explained by the nucleation of Ni crystallites at this thickness, which contributes an additional roughness to the Ti-on-Ni interface. When the thickness of Ni layer is well beyond the critical thickness, the Ti-on-Ni interface becomes smoother as predicted by the wetting condition due to the different surface free energy of Ti and Ni. This investigation should provide useful information to the fabrication of Ni/Ti supermirrors and the Ni/Ti multilayer mirrors working in the water-window soft X-ray region, where stacks of thins films having nanometer-scale thicknesses are needed to be deposited.

AUTHOR INFORMATION

Corresponding Author

*E-mail: wangzs@tongji.edu.cn.

Notes

The authors declare no competing financial interest.

ACKNOWLEDGMENTS

This research has been supported by the 973 program (Grant No. 2011CB922203), National Nature Science Foundation of China (Grant No. 10825521, 11075118), and Fundamental Research Funds for the Central Universities. We thank Dr.

Kawal J. S. Sawhney for helpful discussions. We also gratefully acknowledge Andrew Malandain for his support during the setup of the experiment.

■ REFERENCES

(1) Kumar, M. S.; Böni, P.; Clemens, D. *J. Appl. Phys.* **1998**, *84*, 6940−6942.
(2) Padiyath, J.; Stahn, J.; Horisberger, M.; Böni, P. *Appl. Phys. Lett.* **2006**, *89*, 113123/1−113123/3.
(3) Grimmer, H.; Böni, P.; Breitmeier, U.; Clemens, D.; Horisberger, M.; Mertins, H.-Ch; Schäfers, F. *Thin Solid Films* **1998**, *319*, 73−77.
(4) Mertins, H.-Ch; Schäfers, F.; Grimmer, H.; Clemens, D.; Böni, P.; Horisberger, M. *Appl. Opt.* **1998**, *37*, 1873−1882.
(5) Savage, D. E.; Schimke, N.; Phang, Y.-H.; Lagally, M. G. *J. Appl. Phys.* **1992**, *71*, 3283−3293.
(6) Gupta, M.; Amir, S. M.; Gupta, A.; Stahn, J. *Appl. Phys. Lett.* **2011**, *98*, 101912/1−101912/3.
(7) Paul, A.; Lodha, G. S. *Phys. Rev. B: Condens. Matter Mater. Phys.* **2002**, *65*, 245416/1−245416/9.
(8) Bajt, S.; Stearns, D. G.; Kearney, P. A. *J. Appl. Phys.* **2001**, *90*, 1017−1025.
(9) Ay, M.; Schanzer, C.; Wolff, M.; Stahn, J. *Nucl. Instrum. Methods Phys. Res., Sect. A* **2006**, *562*, 389−392.
(10) Takenaka, H.; Ito, H.; Nagai, K.; Muramatsu, Y.; Gullikson, E.; Perera, R. C. C. *Nucl. Instrum. Methods Phys. Res., Sect. A* **2001**, *467−468*, 341−344.
(11) Hino, M.; Sunohara, H.; Yoshimura, Y.; Maruyama, R.; Tasaki, S.; Yoshino, H.; Kawabata, Y. *Nucl. Instrum. Methods Phys. Res., Sect. A* **2004**, *529*, 54−58.
(12) Clemens, B. M. *Phys. Rev. B: Condens. Matter Mater. Phys.* **1986**, *33*, 7615−7624.
(13) Hollanders, M. A.; Thijsse, B. J.; Mittemeijer, E. J. *Phys. Rev. B: Condens. Matter Mater. Phys.* **1990**, *42*, 5481−5494.
(14) Bhatt, P.; Sharma, A.; Chaudhari, S. M. *J. Appl. Phys.* **2005**, *97*, 043509/1−043509/8.
(15) Bhatt, P.; Prakash, R.; Chaudhari, S. M.; Reddy, V. R.; Phase, D. M. *J. Nanosci. Nanotechnol.* **2007**, *7*, 2081−2086.
(16) Bhatt, P.; Chaudhari, S. M.; Fahlman, M. *J. Phys.: Condens. Matter* **2007**, *19*, 376210/1−376210/11.
(17) Gupta, R.; Gupta, M.; Kulkarni, S. K.; Kharrazi, S.; Gupta, A.; Chaudhari, S. M. *Thin Solid Films* **2006**, *515*, 2213−2219.
(18) Singh, S.; Basu, S.; Bhatt, P.; Poswal, A. K. *Phys. Rev. B: Condens. Matter Mater. Phys.* **2009**, *79*, 195435/1−195435/9.
(19) Soyama, K.; Suzuki, M.; Hazawa, T.; Moriai, A.; Minakawa, N.; Ishii, Y. *Phys. B (Amsterdam, Neth.)* **2002**, *311*, 130−137.
(20) Shinjo, T.; Keune, W. *J. Magn. Magn. Mater.* **1999**, *200*, 598−615.
(21) Bedzyk, M. J.; Bilderback, D. H.; Bommarito, G. M.; Caffrey, M.; Schildkraut, J. S. *Science* **1988**, *241*, 1788−1791.
(22) Bedzyk, M. J.; Bommarito, G. M.; Schildkraut, J. S. *Phys. Rev. Lett.* **1989**, *62*, 1376−1379.
(23) Kawamura, T.; Takenaka, H. *J. Appl. Phys.* **1994**, *75*, 3806−3809.
(24) Yang, S.-H.; Mun, B. S.; Mannella, N.; Kim, S.-K; Kortright, J. B.; Underwood, J.; Salmassi, F.; Arenholz, E.; Young, A.; Hussain, Z.; Van Hove, M. A.; Fadley, C. S. *J. Phys.: Condens. Matter* **2002**, *14*, L407−L420.
(25) Tiwari, M. K.; Sawhney, K. J. S.; Lee, T.-L.; Alcock, S. G.; Lodha, G. S. *Phys. Rev. B: Condens. Matter Mater. Phys.* **2009**, *80*, 035434/1−035434/5.
(26) Ghose, S. K.; Dev, B. N. *Phys. Rev. B: Condens. Matter Mater. Phys.* **2001**, *63*, 245409/1−245409/11.
(27) Gupta, A.; Kumar, D.; Meneghini, C. *Phys. Rev. B: Condens. Matter Mater. Phys.* **2007**, *75*, 064424/1−064424/6.
(28) Li, W. B.; Zhu, J. T.; Ma, X. Y.; Li, H. C.; Wang, H. C.; Sawhney, K. J. S.; Wang, Z. S. *Rev. Sci. Instrum.* **2012**, *83*, 053114/1−053114/5.
(29) Parratt, L. G. *Phys. Rev.* **1954**, *95*, 359−369.
(30) Tiwari, M. K.; Lodha, G. S.; Sawhney, K. J. S. *X-Ray Spectrom.* **2010**, *39*, 127−134.